Version of Record: https://www.sciencedirect.com/science/article/pii/S0926337320311346
Manuscript_a228ec21ee95d50c7d3676bb3971634e

# First demonstration of phosphate enhanced atomically dispersed bimetallic FeCu catalysts as Pt-free cathodes of high temperature phosphoric acid doped polybenzimidazole fuel cells

*Yi Cheng[#a], Mengen Wang[b], Shanfu Lu[c], Chongjian Tang[a], Xing Wu[a], Jean-Pierre Veder[d], Bernt Johannessen[e], Lars Thomsen[e], Jin Zhang[c], Shi-ze Yang[b,f*], Shuangyin Wang[g,*], San Ping Jiang[h,*]*

[a]Department of Environmental Engineering, School of Metallurgy and Environment, Central South University, Changsha 410083, PR China
[b]Center for Functional Nanomaterials, Brookhaven National Laboratory, Upton, NY 11973, United States
[c]Beijing Key Laboratory of Bio-inspired Energy Materials and Devices, School of Space and Environment, Beihang University, Beijing 100191, PR China
[d]John de Laeter Centre, Curtin University, Perth, WA 6102, Australia
[e]Australian Synchrotron, Clayton, Victoria 3168, Australia
[f]Materials Science and Technology Division, Oak Ridge National Laboratory, Oak Ridge, TN 37831, United States
[g]State Key Laboratory of Chem/Bio-Sensing and Chemometrics, College of Chemistry and Chemical Engineering, Hunan University, Changsha 410082, PR China
[h]WA School of Mines: Minerals, Energy and Chemical Engineering, Curtin University, Perth, WA 6102, Australia

**Abstract:** Phosphate poisoning of Pt electrocatalysts is one of the major barriers that constrains the performance of phosphric acid-doped polybenzimidazole (PA/PBI) membrane fuel cells. Herein, we developed new atomically dispersed bimetallic FeCu coordinated with nitrogen-doped carbon nanotubes (FeCu/N-CNTs) as Pt-free fuel cell oxygen reduction reaction (ORR) electrocatalysts. The cell with FeCu/N-CNTs cathodes delivers a peak power density of 302 $mWcm^{-2}$ at 230°C, similar to that using Pt/C electrocatalysts (1 $mg_{Pt}cm^{-2}$) but with a much better stability. In contrast to phosphate poisoning of Pt/C, FeCu/N-CNTs show PA enhanced activities. DFT calcualtions indicate that phosphate promotion effect results from the stronger binding of phosphate on Cu sites, which decreases the activation energy barrier for the cleavage of the $O_2$ double bond and provides local protons to facilitate the proton-coupled electron transfer ORR. The results also show that FeCu/N-CNTs have a much better activity for ORR as

comapre to Fe single atom catalysts coordinated with nitrogen-doped carbon nanotubes, Fe/N-CNTs. This study demonstrates the promising potential of bimetallic FeCu/N-CNTs as true Pt-free, highly active and durable cathodes of PA/PBI based high temperature polymer electrolyte fuel cells.

**Keywords:** high temperature polymer electrolyte membrane fuel cells, phosphate promotion effect, atomically dispersed bimetallic FeCu catalysts, oxygen reduction reaction, Pt-free cathodes.

## 1 Introduction

Fuel cells such as polymer electrolyte membrane fuel cells (PEMFCs) are clean and efficient power sources that are applicable for portable electronic devices[1-3]. However, PEMFCs, running at temperatures lower than 100 $^{o}$C using Nafion membranes are challenged by the system's complexity for water and heat management, dependence on high purity hydrogen, and the high investment needed in hydrogen transportation and distribution infrastructures[4]. Another critical issue is the use of precious platinum (Pt) metal catalysts. Pt has very limited resources and the high cost and scarcity of precious Pt seriously limit the practical and wide application of Nafion membrane based low temperature PEMFCs technologies[5]. Increasing the operational temperature to over 100 $^{o}$C, i.e., high temperature PEMFCs (HT-PEMFCs), will bring a number of advantages, such as improved reaction kinetics at both the cathode and anode, simplified water and heat management systems, significantly alleviated poisoning by CO, $SO_2$, etc. These merits will allow the HT-PEMFCs to use reformed hydrogen from methanol or

ethanol on board without a need for CO clean-up, thus significantly reducing the capital investment in hydrogen transportation and filling station infrastructure [6-9].

Due to the operation at elevated high temperature, phosphoric acid ($H_3PO_4$, PA) is the state-of-the-art proton carrier for PA doped polybenzimidazole (PA/PBI) membrane-based HT-PEMFCs[6, 10]. Similar to Nafion-membrane based low temperature PEMFCs, Pt is also the most common and popular electrocatalyst for the PA/PBI based HT-PEMFCs. However, phosphate ions adsorb strongly on the Pt surface and thus hinder the catalytic process, resulting in poor cell performance despite the high Pt loading applied[11-14]. He et al. studied the effect of PA on the electrochemical activity of Pt and found that the kinetic current for oxygen reduction reaction (ORR) decreases dramatically on Pt and PtSn electrocatalysts after the addition of a small amount of PA (i.e., 1 mM) into a perchloric acid solution[11]. Extensive in-operando X-ray absorption spectroscopy investigations on Pt/C fuel cell cathode catalysts showed the significant coverage of PA anions on the Pt surface at a wide cell voltage of 0.8-0.2 V[14]. The adsorbed phosphate poisons the activity of Pt-based electrocatalysts and substantially retards the ORR kinetics, leading to the reduced performance and stability of PA/PBI membranes-based PEMFCs[11, 15-17]. Zhang et al observed the substantial agglomeration of Pt nanoparticles (NPs) of the Pt/C cathodes of PA/PBI membrane cells after operation at 200 $^oC$ for 2000 h due to the strong adsorption of PA and the grain growth of Pt/C catalysts led to the significant degradation of the PA/PBI based membrane cells[18]. The poisoning of PA on the Pt-based electrocatalysts is one of the main reasons for the much lower power output of the PA/PBI based HT-PEMFC as compared to that of Nafion membrane based PEMFCs[6].

Nitrogen coordinated Fe single atoms have been generally recognized as one of the most promising alternatives to replace Pt-based catalysts in PEMFCs [19-24]. Fe single atom catalysts

(SACs) showed ORR performance close to Pt/C, but there is a concern of the potential structural damage of the Nafion membranes due to the leached Fe ions[22-25]. Most recently, we found that single-phased Fe SACs embedded in N-coordinated graphene (FeSAC-G) showed a better stability as compared to Pt/C catalysts, but the power output of the cells with FeSAC-G is lower than that using Pt/C electrocatalysts, tested at elevated temperature of 230 $^{o}$C[26].

Heme copper oxidases (HCOs), containing a heme that functions as oxygen binding sites and a closely associated copper that play the role to assist O=O double bonding breakage, is one of the most efficient oxidase that can directly reduce molecular $O_2$ to water through 4-electron process[27]. This has led to the investigations in the integrated heme and copper center to obtain the high performance ORR catalysts by mimicking HCOs[28, 29]. The higher ORR activity has been attributed to the higher redox potential and rich electron density in the *d* orbital of copper [27]. Based on this principle, we designed new atomically dispersed bimetallic Fe and Cu atoms anchored on nitrogen doped carbon nanotubes (FeCu/N-CNTs) as Pt-free electrocatalysts for ORR in the PA/PBI membrane-based HT-PEMFCs. The results demonstrate for the first time that in contrast to the adsorption and poisoning of phosphate to Pt-based electrocatalysts, phosphate enhances the electrocatalytic activity of FeCu/N-CNTs for ORR. The experimental and theoretical investigation reveal that phosphate strongly binds on the atomic Cu sites, which facilitate the ORR reaction on the adjacent atomic iron sites. These findings provide a new direction in the design of new class of Pt-free electrocatalysts with high activity and stability for PA-based HT-PEMFCs.

## 2 Experimental Section

### *2.1 Materials synthesis*

CNTs with diameter less than 8 nm were obtained from Nanostructured & Amorphous Materials, USA. CNTs (0.2 g) were dispersed in 200 mL $HNO_3$ (68%, Alfa Aesar) by ultrasonication and refluxed at 160 $^oC$ for 12 h before being centrifuged at 5000 rpm. The solid powder was washed with DI water three times and denoted as O-CNTs. Atomically dispersed bimetallic Fe and Cu atoms anchored on nitrogen doped CNTs catalysts were synthesized through a soft-template method modified from our previous reported method for synthesis of single-phased Ni SACs embedded in N-CNTs[26]. Hemin porcine (HP, $C_{34}H_{32}ClFeN_4O_4$, Sigma-Aldrich), copper (II) acetylacetonate (CuAC, $Cu(C_5H_7O_2)_2$, Sigma Aldrich), dicyandiamide ($C_2H_4N_4$, DICY, Sigma Aldrich) were purchased and used without further treatment. HP and CuAC were mixed with $C_2H_8N_2$ (10 g) with the addition of 20 mL ethanol, followed by grinding till the mixture was dried. The addition of ethanol and grinding process was repeated for 4 times. Subsequently, the mixed powder was heated at 350 $^oC$ for 3 h and then at 650 $^oC$ for 3 h before being heated at 900 $^oC$ for 1 h under Ar with a flow rate of 50 mL $min^{-1}$. The as-synthesized black powder was washed with 2 M $H_2SO_4$ at 80 $^oC$ for three times to remove the metallic NPs which could be formed during the pyrolysis process. The as-synthesized bimetallic FeCu on nitrogen coordinated CNTs was denoted as FeCu/N-CNTs. The electrocatalysts embedded in N-CNTs with HP and CuAC with Fe:Cu atomic ratios of 8:1; 4:1, 2:1, 1:1 and 1:0 were prepared and were denoted as FeCu(X:Y) with X:Y = 8:1, 4:1, 2:1, 1:1 and 1:0, respectively.

*2.2 Characterization*

Morphology of the catalysts was studied by transmission electron microscopy (TEM) and high angle annular dark field (HAADF) scanning TEM (STEM) with elemental mapping on a Titan G2 60-300 at 80 kV. The annular dark field images (ADF) were collected using a Nion

UltraSTEM100 microscope operated at 60 kV at a beam current of 60 pA. The convergence half angle of the electron beam was set to 30 mrad and the inner collection half angle of the ADF images was 51 mrad. Diffraction data was collected with a Bruker D8 Advance diffractometer operated at 40 kV and 40 mA with Cu Kα ($\lambda$ = 1.5406 Å) in the range of 20-90° 2$\theta$. X-ray photoelectron spectroscopy (XPS) were conducted on a Kratos Axis Ultra DLD spectrometer using a monochromatic AlKα (1486.6 eV) irradiation source operated at 225 W.

X-ray absorption spectroscopy (XAS) measurements were performed at the wiggler XAS Beamline (12ID) at the Australian Synchrotron in Melbourne, Australia using a set of liquid nitrogen cooled Si(111) monochromator crystals. With the beamline optics employed (Si-coated collimating mirror and Rh-coated focussing mirror) the harmonic content of the incident X-ray beam was negligible. XAS measurements were performed at the Fe K-edge (7.1 keV) at < 10 K to minimize thermal disorder and to ensure that the samples were not radiation damaged (This was confirmed via repetitive quick scanning of the absorption edge for up to 2 hours, i.e., 12 scans. Note that a single complete XAS scan took ~1 h). For these samples were prepared as pellets via mechanical grinding in a cellulose binder using a mortar/pestle. Both fluorescence and transmission spectra were recorded depending on the concentration of Fe in each sample (the validity of this approach was confirmed by comparing the fluorescence and transmission spectrum for one of the samples for which both methods yielded comparable signal-to-noise data).

Data processing and analysis were performed following standard methods [30]. The extended X-ray absorption fine structure (EXAFS) data was isolated using the Athena software[31]. The normalised EXAFS was then Fourier transformed over a photoelectron

momentum (*k*) range of 2.0-14.0 $Å^{-1}$. The coordination shell(s) to be analysed were isolated by inverse transforming over a non-phase-corrected radial distance (R) range of 0.7-2.7 Å.

X-ray absorption near edge structure spectroscopy (XANES) measurements below photon energies of 2,500 eV were conducted at the Soft X-Ray beamline of the Australian Synchrotron[32]. These measurements were carried out at room temperature under ultra-high vacuum (UHV) conditions with a base pressure of 5 x $10^{-10}$ mbar or better. All spectra were obtained in total electron yield (TEY) mode. The XANES spectra were recorded at the Fe L-edge (700-740 eV), C K-edges (280-320 eV) and N K-edges (395-420 eV). All XANES spectra were processed and normalized using the QANT software program developed at the Australian Synchrotron[33]. X-ray energy calibrations were achieved by applying the offset required to shift the simultaneously measured reference spectra of iron foil and boron nitride powder to its known energy. Intensities have been normalized with respect to impinging photon flux. Standard chemicals including iron phthalocyanine and iron foil were tested as reference materials. The iron content was obtained by inductively coupled plasma optical emission spectrometry (ICP-OES) following the procedures reported[34]. The solution for ICP-OES test was prepared by dissolution of the solid yield from burning 50 mg catalysts in a crucible with $HNO_3$ acid.

*2.3 Electrochemical and fuel cell test*

Electrochemical measurements were conducted in a standard electrochemical cell using a Princeton potentiostat (Versastat3, USA). Graphite rod and saturated calomel electrode (SCE) with electrolytic bridge were used as the counter and reference electrodes. Linear scan voltammetry (LSV) curves of FeCu/N-CNTs and Pt/C (50% Pt, JM) were obtained in $O_2$-saturated 0.1M $HClO_4$ solution with and without addition of PA using rotating ring disk

electrodes with rotating rate of 1600 rpm. The IR-corrected Tafel plots were recorded at a scan rate of 1 mV $s^{-1}$ with the electrode initially conditioned at current density of 0.5 mA $cm^{-2}$ for 5 min. The FeCu catalyst loading was ~36 μg $cm^{-2}$ for FeCu-N-CNTs, and Pt loading was 25 μg $cm^{-2}$ for Pt/C. All potentials in the present study were given versus RHE reference electrode (E = $E_{SCE}$ + 0.247 + 0.059 pH, here 0.247 V is the potential for SCE at 20 ºC). MEAs with an active area of 4 $cm^2$ were fabricated by sandwiching the $SiO_2$ doped PA/PBI composite membrane between two gas diffusion electrodes with Pt/C anode and FeCu(4:1) cathode followed by hot-pressing at 4.9 MPa and 180 ºC for 10 minutes. The fabrication of MEAs can be found in previous publications[35]. The Pt loading of the anode was 1.0 $mg_{Pt}$ $cm^{-2}$. The performance of PA/PBI based composite membrane cells was measured at 230 ºC in $H_2$ and $O_2$ with flow rates of 100 mL $min^{-1}$. Stability test was undertaken at a cell voltage of 0.5 V and 230 °C. For comparison, a fuel cell using Pt/C catalysts on both anode and cathode with Pt loading of 1.0 $mg_{Pt}$ $cm^{-2}$ was also tested following the same procedure. The accelerated durability tests were evaluated using the cyclic voltammograms (CVs) in a $N_2$-saturated 0.1 M $HClO_4$ electrolyte with a sweep rate of 50 mV $s^{-1}$ at the potential range of 0.1-1.0 V for 5000 cycles.

*2.4 Computational Methods*

Density functional theory (DFT) calculations were performed using the projector augmented wave method implemented in the Vienna Ab initio simulation package (VASP)[36, 37]. The PBE functional was used to describe the electronic exchange and correlation effects[38]. For Fe doped graphene, the system consists of a single layer graphene in a 14.81 Å × 14.81 Å × 15 Å cell and the Brillouin zone was sampled with a 3×3×1 grid. For Fe-Cu doped graphene, a 29.62 Å × 14.81 Å × 15 Å cell was used to avoid interaction between the Fe-Cu sites in neighboring cells and the Brillouin zone was sampled with a 2×4×1 grid. All atoms were allowed to relax in

the structural optimization until forces were smaller than 0.01 eV/Å. The absorption energies of *OOH, *O, and *OH were calculated according to

$$\Delta E_{*OOH} = E_{sub+*OOH} - E_{sub} - \left(2E_{H_2O} + \frac{3}{2}E_{H_2}\right) \quad (1)$$

$$\Delta E_{*O} = E_{sub+*O} - E_{sub} - \left(E_{H_2O} - E_{H_2}\right) \quad (2)$$

$$\Delta E_{*OH} = E_{sub+*OH} - E_{sub} - \left(E_{H_2O} - \frac{1}{2}E_{H_2}\right) \quad (3)$$

where $E_{sub}$, $E_{sub}$ + *OOH, $E_{sub}$ + *O, $E_{sub}$ + *OH are the ground state energies of a clean surface and surfaces with *OOH, *O, and *OH adsorbed[39].

## 3 Results and Discussion

### *3.1 Activity of FeCu/N-CNTs for ORR*

FeCu/N-CNTs with different Fe:Cu atomic ratios were synthesized through pyrolysis of the dicyandiamide in the presence of hemin porcine and copper(II) acetylacetonate after a subsequent acid treatment (Figure 1A). The ORR activities are closely related with the Fe:Cu ratios of FeCu/N-CNTs catalysts, as shown in the linear scan voltammetry (LSV) curves, measured in 0.1 M $HClO_4$ electrolyte (Figure 1B). The best results were obtained on FeCu/N-CNTs with Fe:Cu ratio of 4:1, FeCu(4:1), achieving an on-set potential of 0.960 V vs RHE (without specification, the potentials in following sections are referred to RHE) and a half-wave potential ($E_{1/2}$) of 0.811 V. This is close to on-set potential of 0.980 and $E_{1/2}$ of 0.822 V obtained on Pt/C catalyst. FeCu(4:1) is among one of the most active non-noble metal based ORR catalysts reported in acid electrolyte (Table S1). For example, Dai group developed an iron single atom catalyst, showing a $E_{1/2}$ of 0.81 V with enhanced stability in acidic electrolytes[40].

Li et al synthesized an atomically dispersed Fe-$N_x$/C sites exhibits ORR activity with $E_{1/2}$ of 0.812 in 0.5 M $H_2SO_4$[41]. The electrocatalytic activity of FeCu(4:1) is also better than the constitute single Fe and Cu atom catalysts. For the ORR on Fe/N-CNTs SACs, $E_{1/2}$ is 0.801 V, while Cu/N-CNTs SACs, FeCu(0:1), is very poor for ORR with on-set potential of 0.80 V and $E_{1/2}$ of 0.63 V, which is consistent with the poor ORR activity of Cu-N-C in acid electrolyte[24]. Further decrease of the Fe:Cu ratio resulted in the decrease of the activity due to a severe aggregation of the Fe and Cu atoms to form NPs (Figure S1).

The $H_2O_2$ yield calculated from the ring current of the rotating ring-disk electrode studies is ~2-3% for FeCu(4:1), which is lower than 6-7% for FeCu(1:0) and 8-10% for Pt/C (Figure 1D). The electron transfer number for FeCu(4:1) is 3.8-4.0 in the potential range of 0.2-0.7 V, very close to 3.8-3.9 for that on Pt/C. This indicates the 4-electron transfer process of ORR on FeCu(4:1) catalysts. Tafel slope for the reaction on FeCu(4:1) and FeCu(1:0) is 105 mV $dec^{-1}$, lower than 120 mV $dec^{-1}$ of Pt/C (Figure 1E), indicating the slightly higher ORR kinetics on FeCu(1:0) and FeCu(4:1). This is comparable to that of atomically dispersed Fe-$N_x$ species on porous porphyrinic triazine-based frameworks with Tafel slope of ~81 mV $dec^{-1}$[42, 43].

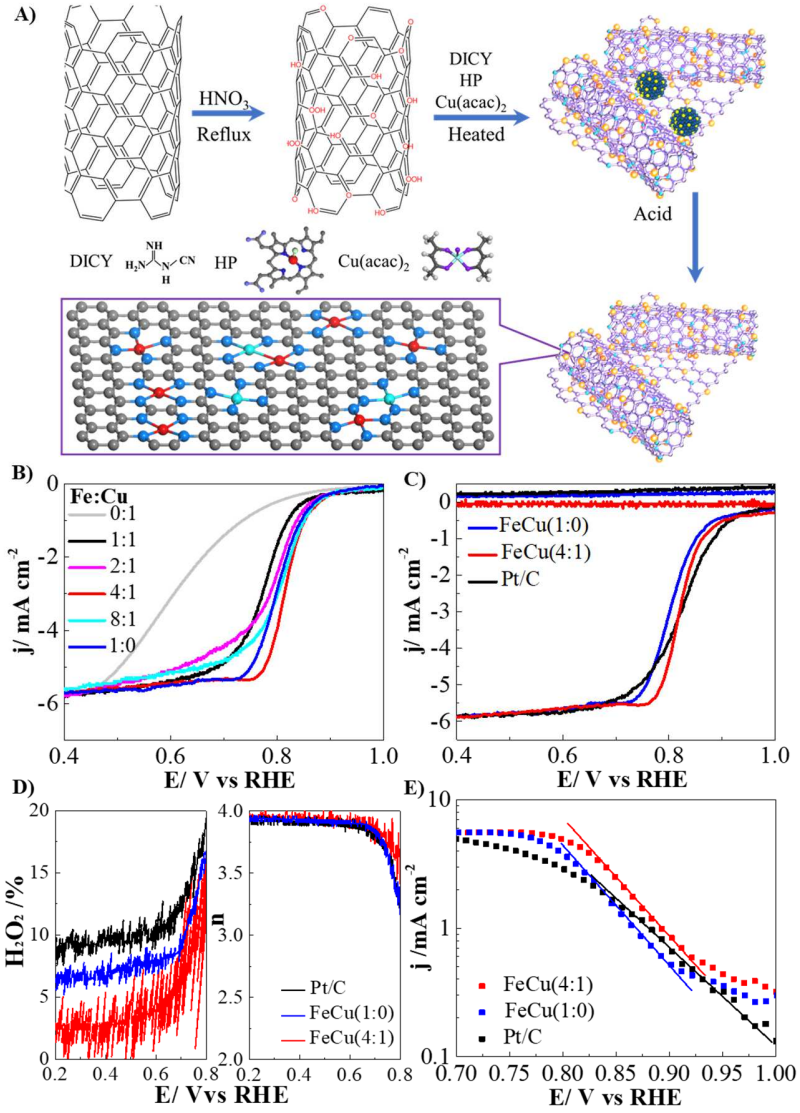


**Figure 1.** A) Scheme for FeCu-N-CNTs synthesis; B) Linear scan voltammetry (LSV) of FeCu/N-CNTs with different Fe/Cu atomic ratios in $O_2$-saturated $HClO_4$ solution; C) LSV of FeCu(4:1), FeCu(1:0) and Pt/C in $O_2$-saturated $HClO_4$ solution; D) $H_2O_2$ yield and calculated electron transfer number of FeCu(4:1), FeCu(1:0) and Pt/C during the ORR; E) Tafel slope of FeCu(4:1), FeCu(1:0) and Pt/C for ORR. The catalyst loading of FeCu was 36 μg $cm^{-2}$, and Pt loading was 36 μg $cm^{-2}$. The double layer current was deducted and the current was IR corrected.

With the addition of 0.2 M PA in 0.1 M $HClO_4$ solution, the on-set potential and $E_{1/2}$ of ORR on Pt/C electrocatalysts were shifted negatively by 14 mV and 26 mV, respectively (Figure 2A). The limiting current density measured at 0.8 V also decreased by 30% from 2.79 mA $cm^{-2}$ in 0.1 M $HClO_4$ to 1.91 mA $cm^{-2}$ in 0.2 M PA+0.1 M $HClO_4$. The reduced limiting current

density with the addition of PA in the electrolyte is most likely caused by the lower diffusion coefficient and $O_2$ solubility as well as the higher kinematic viscosity of PA relative to that in pristine 0.1 M $HClO_4$ solution. This effectively leads to a decrease in the mass-transfer-limited current of the ORR [12, 44]. The negative shift in $E_{1/2}$ and decrease in the limiting current density indicate the adsorption and poisoning of PA on the active sites of Pt for ORR in acidic solution, consistent with that reported in the literatures[11-14]. Very different from Pt/C, the electrocatalytic activity of FeCu(4:1) for ORR increases with the addition of PA. The $E_{1/2}$ of FeCu(4:1) for ORR is 0.830 V in 0.2 M PA + 0.1 M $HClO_4$ solution, which is 18 mV higher than 0.812 V measured in 0.1 M $HClO_4$ solution (Figure 2B) and 34 mV higher than 0.796 V measured on Pt/C under identical conditions (Figure 2C). Polarization density at 0.8 V for ORR on FeCu(4:1) is 4.3 mA $cm^{-2}$, which is ~2 times higher than 2.2 mA $cm^{-2}$ on Pt/C (Figure 2C).

The corresponding Tafel slope for ORR on FeCu(4:1) catalyst also decreased from 105 mV $dec^{-1}$ in 0.1 M $HClO_4$ electrolyte to 98 mV $dec^{-1}$ in 0.2 M PA+ 0.1 M $HClO_4$ solution (Figure 2D), consistent with the reported results[12]. The increase of $E_{1/2}$ and current density, combined with the decrease of the Tafel slope for FeCu(4:1) for ORR in the presence of PA evidently indicates that the presence of PA actually promotes the electrocatalytic activity of bimetallic FeCu/N-CNTs catalysts. The accelerated durability tests of FeCu(4:1) reveal that the $E_{1/2}$ negatively shifted by 12 mV after 5000 cycles at scan rate of 50 mV $s^{-1}$, which is lower than a negative shift of 38 mV for Pt/C tested under identical conditions (Figure S2), indicating a higher durability of FeCu(4:1) in comparison to that Pt/C.

FeCu(4:1) and FeCu(1:0) electrocatalysts were selected and applied as cathodes for the PA/PBI composite membrane cells at 230 $^oC$ in $H_2$ and $O_2$ without humidification. Membrane-electrode assemblies (MEAs) with an active area of 4 $cm^2$ were fabricated by

sandwiching a PA/PBI composite membrane between two gas diffusion electrodes with Pt/C anode (Pt loading=1 $mg_{Pt}$ $cm^{-2}$) and FeCu(1:0) and FeCu(4:1) cathode (FeCu metal loading=~0.12 $mg_{FeCu}$ $cm^{-2}$). For comparison, MEAs with Pt/C anode and Pt/C cathodes (Pt loading=1 $mg_{Pt}$ $cm^{-2}$) were also prepared. At 230 ºC, the open circuit voltage of the cell with FeCu(4:1) and FeCu(1:0) cathodes is 0.87-0.89 V, which is slightly lower than the 0.95 V measured on the cell with Pt/C cathode. The cell with FeCu(4:1) cathode achieved a power density 221 mW $cm^{-2}$ at 0.6 V (P@0.6) and the peak power density (PPD) of 302 mW $cm^{-2}$, which is identical to that using Pt/C cathode, but significantly higher than the 115 and 240 mW $cm^{-2}$ obtained on the cell with the FeCu(1:0) cathode. The high power output of the cell with FeCu(4:1) cathode as compared to that of FeCu(1:0) indicates the significantly enhanced activity of bimetallic atomic catalysts for ORR, as compared to the monometallic atomic catalysts in PA/PBI composite membrane cells. This is consistent with the significantly enhanced activity of FeCu(4:1) catalyst for ORR in PA-containing 0.1 M $HClO_4$ solution measured at room temperatures (Figure 2B). The cell with FeCu(4:1) cathode also delivered an excellent stability (Figure 2F). The current density of the cell was in the range of 300-320 mA $cm^{-2}$ under a constant cell voltage of 0.5 V at 230 ºC and remained more or less the same after polarization for 100 h. In contrast, the cells with Pt/C cathodes tested at 230 ºC deteriorate rather quickly due to the significant agglomerate of Pt nanoparticles and the poisoning of the phosphate ions, although the cell performance increases initially [26].

The cell with bimetallic FeCu atomic catalyst cathode also show a better performance at low operation temperature as compared to that with Fe single atomic catalyst cathode (Fig.2G). At 160 ºC, the PPD of the cell with FeCu(4:1) cathode is 250 mA $cm^{-2}$, much better than 212 mW $cm^{-2}$ obtained on the cell with Fe single atom catalyst cathode, FeCu(1:0). This indicates that

bimetallic FeCu atomic catalysts show a significant enhanced activity for ORR in a wide range of operation temperature of HT-PEMFCs. The results clearly demonstrate the promising potential of bimetallic FeCu(4:1) as truly Pt-free and high activity and durability cathodes of PA/PBI membranes based HT-PEMFCs.

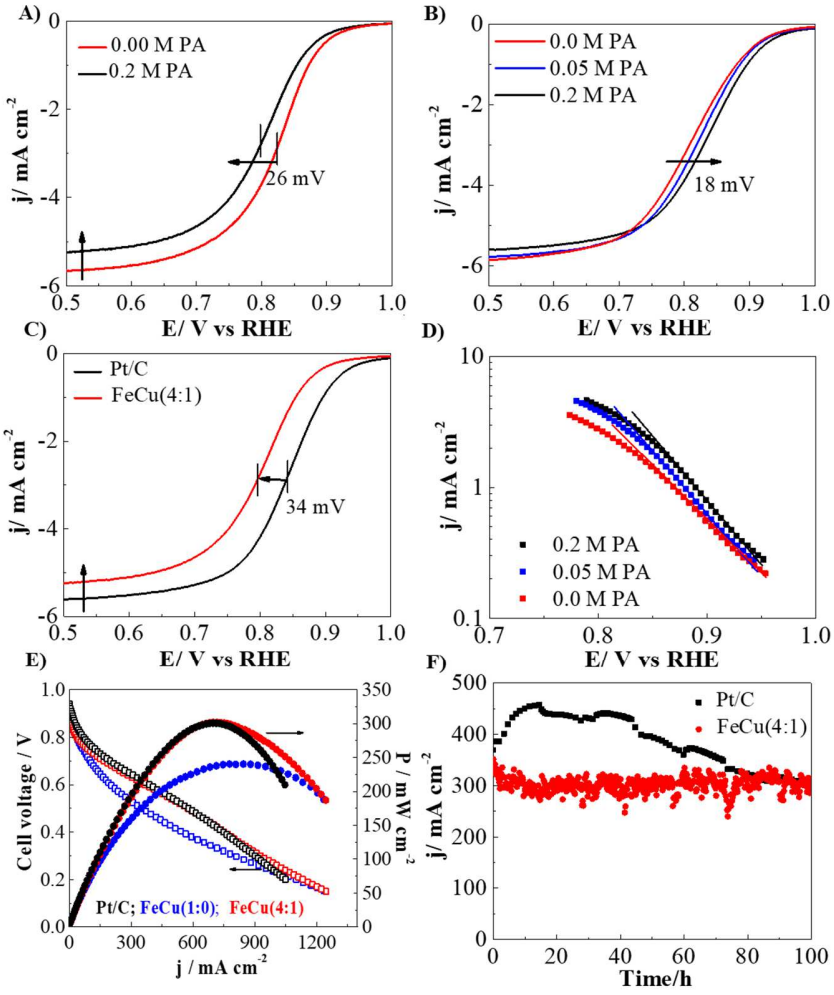

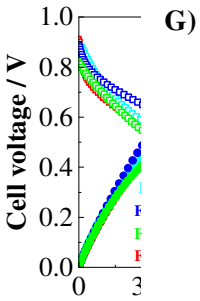


**Figure 2.** LSV of ORR on A) Pt/C, B) FeCu(4:1) in $O_2$-saturated 0.1M $HClO_4$ solution with the addition of PA; C) LSV of ORR on FeCu(4:1) and Pt/C in $O_2$-saturated 0.2 M PA + 0.1 M $HClO_4$ solution; D) Tafel slope curves of ORR on FeCu(4:1) in $O_2$-saturated 0.1M $HClO_4$ solution with the addition of PA. The catalyst loading of FeCu was 36 µg $cm^{-2}$, and Pt loading was 36 µg $cm^{-2}$. E) Polarization and power density curves of PA/PBI composite membrane cells using FeCu(1:0), FeCu(4:1) and Pt/C cathodes at 230 $^oC$; F) cell stability of the cells with FeCu(4:1) cathode at 0.5 V and Pt/C cathode at 0.6 V, and G) Polarization and power density curves of PA/PBI composite membrane cells using FeCu(1:0) and FeCu(4:1) cathodes at 160 and 230 $^oC$. The anode was Pt/C with Pt loading of 1 $mg_{Pt}$ $cm^{-2}$. The cathode loading: Pt loading = 1 $mg_{Pt}$ $cm^{-2}$, total FeCu(1:0) and FeCu(4:1) loading= 4 mg $cm^{-2}$ in which FeCu metal loading was ~0.12 $mg_{FeCu}$ $cm^{-2}$.

The effect of phosphate on the electrochemical activity of monometallic Fe SAC, FeCu(1:0), catalysts for ORR was also investigated and the results are shown in Figure 3. With or without addition of 0.2 M PA in $HClO_4$ solution, the on-set potential and $E_{1/2}$ of ORR on FeCu(1:0) electrocatalysts were essentially identical and the only change is the decrease of the limiting current density measured at 0.8 V for ORR in 0.2 M PA+0.1 M $HClO_4$ as compared to that in 0.1 M $HClO_4$ (Figure 3A). This evidently indicates that the surprising phosphate promoted activity is related to the presence of Cu atoms in the bimetallic FeCu electrocatalysts (Figure 2B). On the other hand, the Tafel slopes observed on both FeCu(1:0) are identical, while for ORR on Pt/C the presence of PA has a minor effect on the Tafel slope (Figure 3B). Monometallic Fe SAC is inert to PA but with no enhancement effect, consistent with previous report[26].

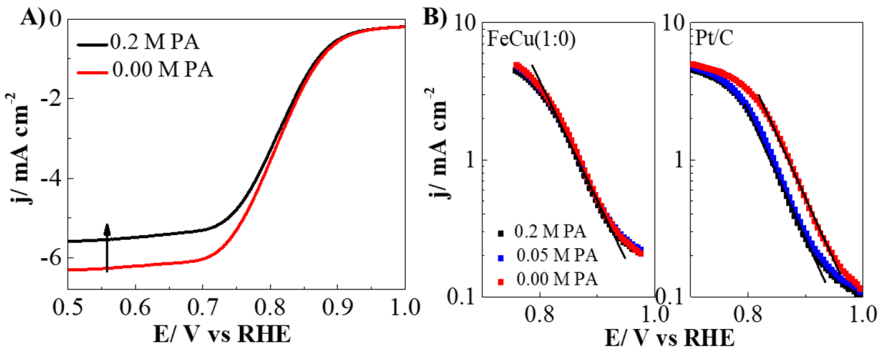


**Figure 3**. A) LSV of ORR on FeCu(1:0) in $O_2$-saturated 0.1M $HClO_4$ solution with the addition of different concentration of PA and B) Tafel slope curves of ORR in $O_2$-saturated 0.1M $HClO_4$ solution with the addition of different concentration of PA on FeCu(1:0) and Pt/C. The catalyst loading of FeCu was 36 μg $cm^{-2}$, and Pt loading was 36 μg $cm^{-2}$.

*3.2 Microstructure of FeCu/N-CNTs*

To understand the high activity and stability of FeCu(4:1) catalysts, detailed structure characterisation was carried out. Figure 4 shows the microstructure of typical FeCu(4:1) and FeCu(1:0) catalysts. Transmission electron microscopy (TEM) and aberration-corrected scanning TEM (AC-STEM) investigations reveal that microstructure of FeCu(4:1) is characterized by CNTs network connected by layers of graphene sheets or amorphous carbon (Figure 4A and B), indicating the growth of graphene-like layers after pyrolysis. The scanning TEM coupled with energy-dispersive X-ray spectroscopy (STEM-EDS) mapping reveals the homogenous distribution of Fe, Cu and N elements on the CNTs-graphene network (Figure 4C). AC-STEM analysis indicates the presence of atomically dispersion Fe and Cu atoms on the CNT or the graphene-like sheets (Figure 4D, E and F). No metallic NPs were observed after acid wash, consistent with the XRD patterns in which no peaks were found that is attributed to Fe, Cu or FeCu alloys NPs (Figure S3). With the increase of Fe:Cu ratio, the decrease of Fe, Cu atomic site density and the increase of FeCu nanoclusters were observed, e.g., nanoclusters formation in

FeCu(1:1) (Figure S4), consistent with the drop of ORR activity (Figure 1B). In the case of FeCu(1:0), similar microstructure was observed. Fe single atoms were uniformly dispersed on the CNT surface or the graphene-like sheets (Figure 4G-I). These results indicate that the addition of Cu atoms leads to the formation of closely adjacent Fe and Cu dual sites or atomically dispersed nanoclusters.

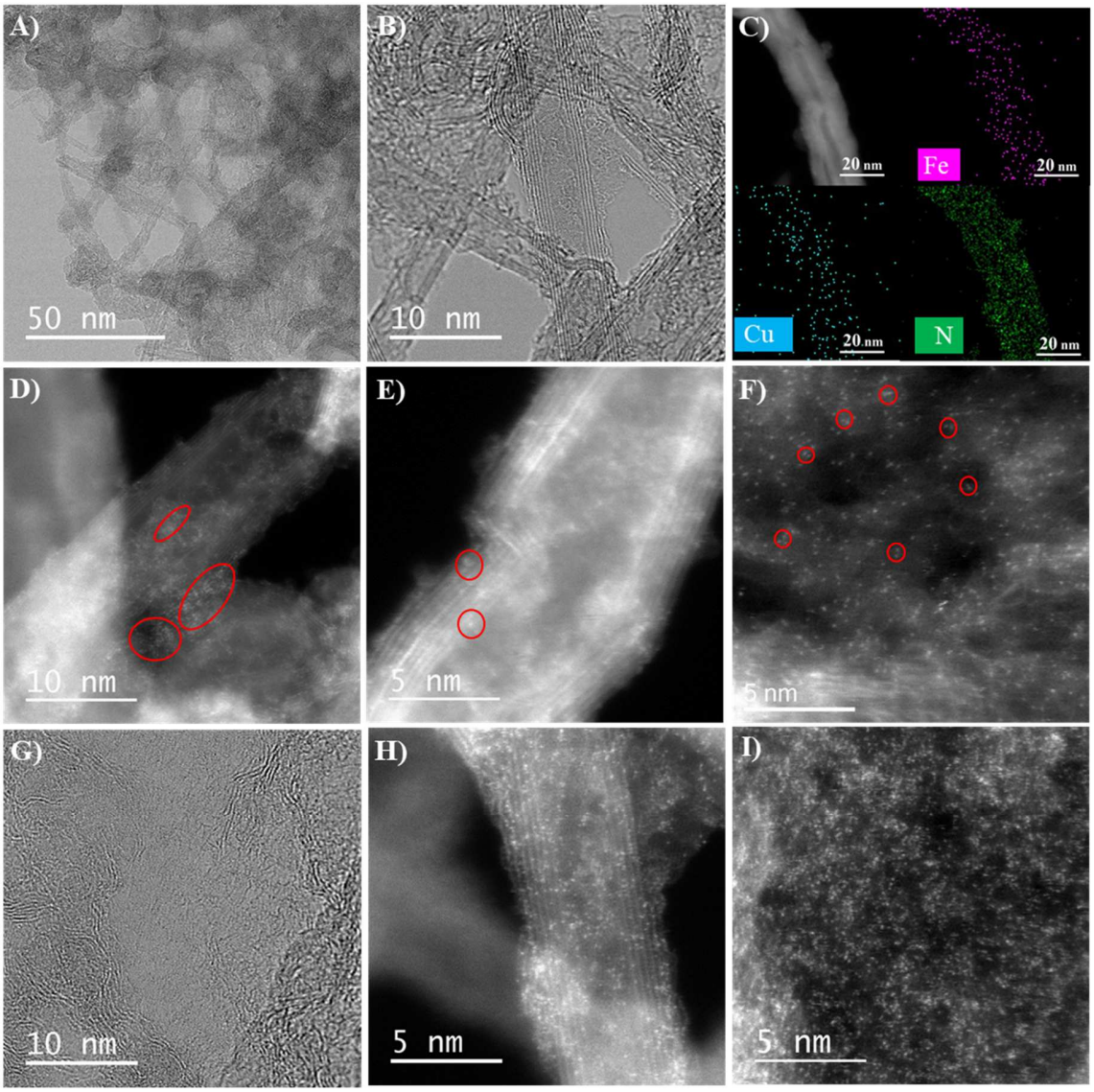


**Figure 4.** A) TEM image; B) high resolution TEM image; C) STEM-EDS mapping; D) and E) AC-STEM of the CNT surface, where circles show the presence of dual sites and isolated atoms;

and F) graphene like sheet, where the circles show the existence of atomically dispersed nanoclusters of FeCu(4:1). G) High resolution TEM image, H) and I) AC-STEM of FeCu(1:0).

The X-ray absorption spectroscopy (X-ray absorption near edge structure, XANES, and X-ray absorption fine structure, XAFS) results are shown in Figure 5A-D. In the case of FeCu(1:0), the peaks located at 401.0 eV, 399.6 eV, 398.3 eV of N K-edge can be assigned to pyridinic-N, pyrrollic-N and graphitic-N coordinated with Fe, respectively (Figure 5A)[45]. For FeCu(4:1), in addition to the similar peaks observed at 401.0 eV, 399.6 eV and 398.3 eV as that of FeCu(1:0), a new peak at 398.7 eV could be due to the formation of Cu-N bonds. The Fe L-edge for FeCu(4:1) is very similar to that of FeCu(1:0), while the slightly increased shoulder at 708.3 eV is attributed to the presence of a small amount of metallic nanoclusters in FeCu(4:1) (Figure 5B). The Fe K-edge of the XANES spectra of FeCu(1:1), FeCu(4:1), FeCu(1:0) and Fe foil indicate that the iron species in FeCu(1:0) and FeCu(4:1) are in Fe(II) state in comparison to that of Fe foil in zero valence and FePc in Fe(III) state (Figure S5). Fourier transform (FT) of the extended XAFS (EXAFS) of the Fe K-edge reveals that the FeCu(1:0) and FeCu(4:1) exhibits a defined shell at 1.6 Å (Figure 5C), which can be attributed to the presence of Fe-N[46, 47]. A tiny peak at 2.1 Å associated with Fe-Fe bond was observed in FeCu(1:0), indicating that majority of Fe species are isolated atoms coordinated with nitrogen. A peak at 2.3 Å for FeCu(4:1) is attributed to the Fe-Fe and Fe-Cu bonds, consistent with the reported Fe L-edge results[48]. With the increase of Fe:Cu ratio to 1:1, the peak at 2.3 Å increases significantly (Figure S6), indicating the increased formation of Fe-Fe and Fe-Cu bonding[49, 50]. Besides, a broad peak around 3.5-5.2 Å observed in the FeCu(4:1) is different from that of Fe foil and FeCu(1:0), indicating the formation of the adjacent Fe and Cu single atoms with a distance

around 4-5 Å[51, 52]. These results indicate that Fe could exist as a Fe-$N_4$ configuration because this is the most energetically favorable structure.

The Cu L-edge of FeCu(4:1) is very different from that of Cu foil, but shows similar feature with that of copper phthalocyanine (CuPc)[53] and $Cu^{2+}$-1,10-phenathroline[54]. This indicates that majority of Cu atoms are coordinated with N to form atomically dispersed Cu atoms rather than Cu nanoclusters with Cu-Cu bond (Figure S7). From the EXAFS data, it is clear that the FeCu sample is significantly different from that of an ordered, metallic material. The pre-edge peaks and the post-edge regions of the XANES of FeCu(4:1) is higher than that of Cu foil, and close to that of reported atomically dispersed Fe-Cu single atom sites (Figure S8A)[48], revealing the oxidation state of the Cu. Specifically, the EXAFS oscillation period is longer than that of metallic Cu. This indicates an environment dominated by Cu bonding to a weak scatterer at a shorter bond-length than that found in metallic Cu (Figure S8B). Moreover, the EXAFS oscillation amplitudes are significantly reduced in the FeCu sample, consistent with a material that is lacking medium to long range atomic order as shown in the Fourier Transformed EXAFS data. The FT of the EXAFS spectra of Cu K-edge (Figure 5D) reveals the formation of atomic Cu sites as indicated at the peak at 1.45 Å, consistent with the Cu L-edge results. Small peaks at 2.3 Å around 4-5 Å indicate the formation of Fe and Cu interactions as indicated in FT of the EXAFS spectra of Fe K-edge. These results further demonstrate the formation of atomically dispersed and nitrogen coordinated dual Fe and Cu diatomic sites on N-CNTs-graphene network in the case of bimetallic FeCu(4:1) catalysts, consistent with the AC-STEM results.

The inductively coupled plasma atomic emission spectroscopy (ICP-AES) results reveal that the Fe content in FeCu(1:0) is 2.8 wt%, and the Fe and Cu content in FeCu(4:1) is 2.52 wt% and 0.48 wt%, respectively. The Fe and Cu atomic ratio is 5.97, higher than the designed ratio of 4:1,

most likely due to the removal of excess Cu nanoclusters by acid treatment. The nitrogen content in FeCu(1:0) and FeCu(4:1) is around 3.94 wt% and 3.93 wt%, respectively through elemental analysis. The high content of N that provide large number of defects could anchor the atomically dispersed Fe and Cu atoms, thus leading to a high density of isolated active sites.

The FeCu(4:1) cathode catalysts before and after fuel cell test were investigated by X-ray photon spectroscopy in order to understand the role of copper in PA promoted ORR (Figure 4E-F). In the figure, FeCu(1:0) and FeCu(4:1) after fuel cell test is denoted as FeCu(1:0)-PA and FeCu(4:1)-PA, respectively. The Fe 2p of the original FeCu(4:1) shows a peak centered at 710.4 eV and 724.1 eV for Fe $2p_{3/2}$ and Fe $2p_{1/2}$, respectively, which is consistent with the XPS spectra of typical Fe-N-C single atom materials reported[55]. The main feature of Fe 2p peaks at 710.4 eV and 724.1 eV for Fe $2p_{3/2}$ and Fe $2p_{1/2}$, respectively, remain unchanged after the cell test, except a small, new feature at 707.5 eV for FeCu(4:1)-PA most likely due to the presence of small amount of FeP[56]. The Cu $2p_{3/2}$ and Cu $2p_{1/2}$ spectra of FeCu(4:1) was observed at 932.4 eV and 952.2 eV, respectively, consistent with the formation of Cu-N bond[57]. However, the Cu $2p_{3/2}$ and Cu $2p_{1/2}$ peaks for FeCu(4:1)-PA were observed at 934.6 eV and 954.5 eV, positively shifted by more than 2 eV in comparison to 932.1 and 952.0 eV observed on pristine FeCu(4:1) before test. These are consistent with the formation of Cu-P or Cu phosphate phase, revealing the strong and preferential binding of the phosphate ions on the Cu single atoms rather than on the Fe single atoms, consistent with that reported in the literature[58-60].

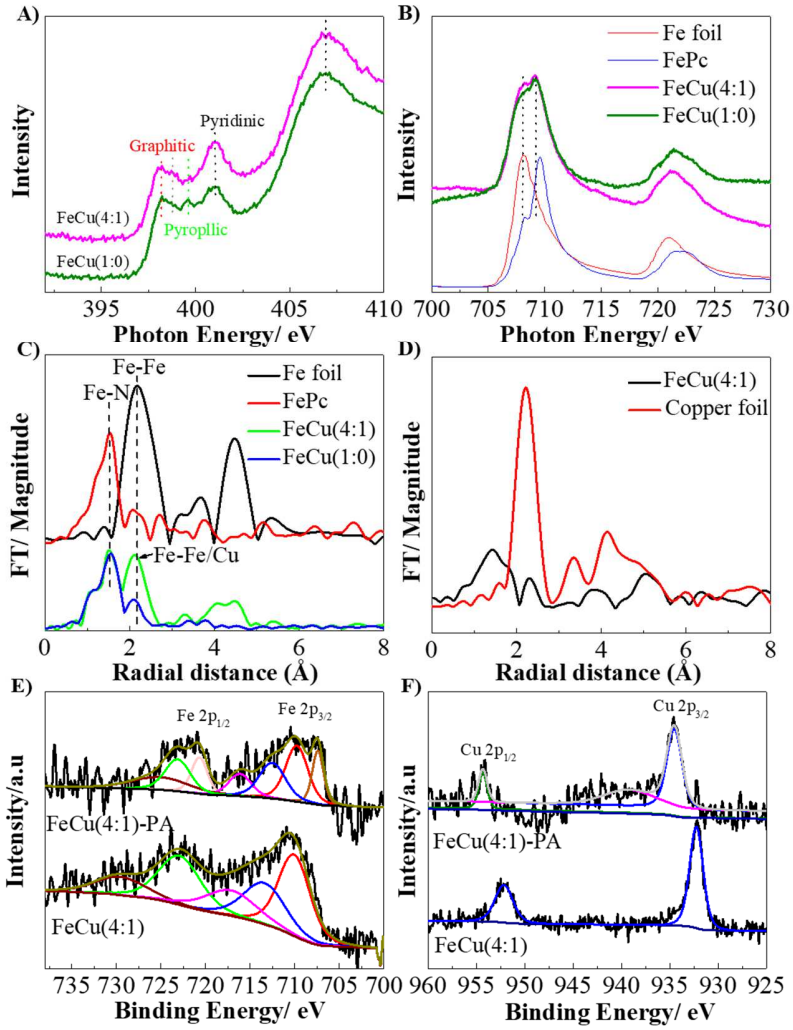


**Figure 5.** A) N K-edge; B) Fe L-edge of the soft X-ray adsorption spectra; C) Fourier transform of EXAFS spectra of FeCu(4:1), FeCu(1:0), FePc and Fe foil; and D) Cu K-edge of FeCu(4:1) and Cu foil. XPS spectra of E) Fe 2p and F) Cu 2p of FeCu(4:1) before and after fuel cell test.

*3.3 Computational simulation*

DFT calculations were performed to determine the potential energy surfaces of FeCu bimetallic catalysts for ORR (Figure 6 and Table 1). It has been indicated that transition metal-$N_4$ configuration is the most energetically favorable structure and is active towards ORR through the four-electron dissociation pathway[61, 62]. The adsorption energies of *OOH, *O,

and *OH were calculated using the Fe-$N_4$ configuration. Cu-$N_4$ center shows a poor ORR activity ($E_{1/2}$=0.61 V, Figure 1B) due to the strong binding of *O on the atomic Cu center (with an energy barrier, ΔE of 2.58 eV). The rate-determining step of ORR on Fe-$N_4$ is the *OOH dissociation step (*OOH→*O) with a ΔE of 1.94 eV (Figure 6B). In order to determine the Fe-Cu doped structure, three configurations with the Fe-Cu distance ($d_{Fe\text{-}Cu}$) of 2.43 Å, 4.38 Å, and 5.05 Å were built (see Figure 6A). In the case of Fe-Cu configuration at $d_{Fe\text{-}Cu}$ = 2.43 Å, the energy barrier for the *OOH→*O is high, 2.58 eV, which is less energy favorable for ORR compared to Fe-$N_4$ sites. This is consistent with the experimental results that the increase of Cu ratio significantly increases Fe-Cu bond, thus leading to the decrease ORR performance (Figure 1B). With the increase of the Fe-Cu distance to 5.05 Å, i.e., the structure with $d_{Fe\text{-}Cu}$ = 5.05 Å, ΔE of the *OOH→O* dissociation step is reduced to 1.89 eV (Figure 6B), indicating the reduced energy barrier of these atomic sites for $O_2$ double bond cleavage. The increased distance between Fe and Cu in the structure implies the decrease in the FeCu ratio in FeCu/N-CNTs catalysts. The results reveal that the enhancement of the ORR activity in FeCu(4:1) is likely due to the formation of atomically dispersed Fe and Cu sites with a favorable distance around 5.05 Å with significantly reduced energy barrier for ORR.

The effect of phosphate on the performance of Fe, Cu doped graphene for ORR was further studied. As shown in Figure S9 and Figure 6B ($d_{Fe\text{-}Cu}$ 5.05 P and FeCu=4.38 P), phosphate adsorbed on the structure with $d_{Fe\text{-}Cu}$ of 4.38 Å and 5.05 Å where phosphate adsorption is much more energy favorable on the Cu site (-1.63 eV), compare to that of 0 eV on the Fe site, which is consistent with the XPS results. ΔE of the *OOH dissociation step is further lowered from 1.98 and 1.89 eV to 1.59 and 1.80 eV for $d_{Fe\text{-}Cu}$ of 4.38 Å and 5.05 Å, respectively for ORR in the presence of phosphate (Figure 6B). The results are clearly consistent with the experimental

studies that the phosphate can strongly adsorb on the surface of the atomic copper sites and promote the ORR on the atomic Fe site.

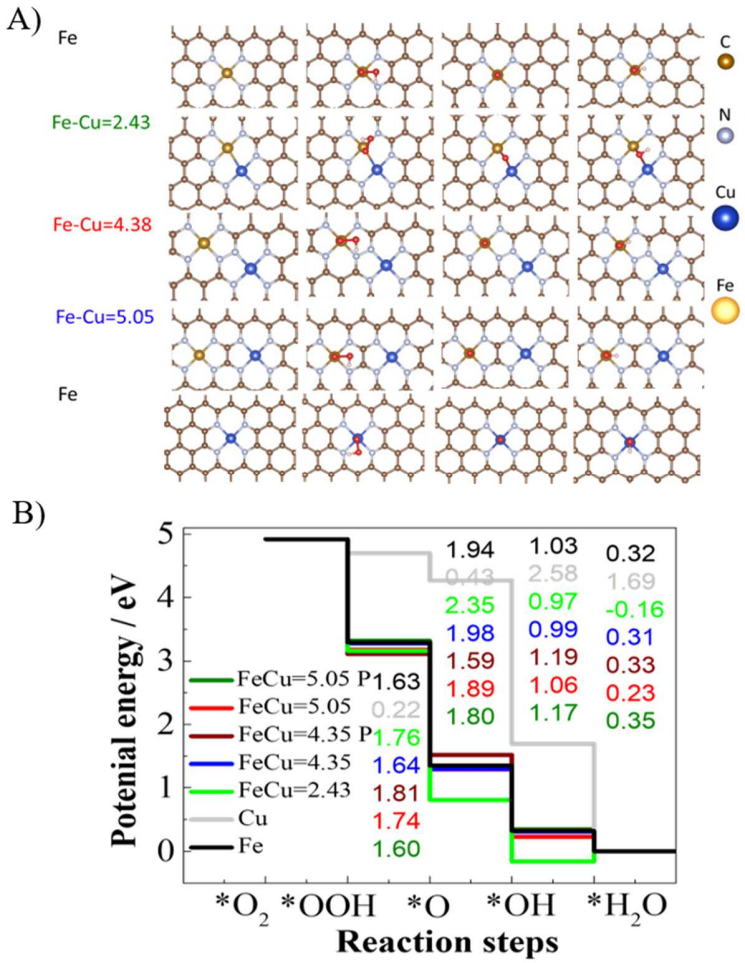


**Figure 6.** A) Top views of structures of the clean and *OOH, *O, *OH adsorbed surfaces of Fe doped graphene, Fe-Cu doped graphene with $d_{Fe\text{-}Cu}$ = 2.43 Å, $d_{Fe\text{-}Cu}$ = 4.38 Å, $d_{Fe\text{-}Cu}$ = 5.05 Å and Cu doped graphene, and B) Potential energy surface for the four-electron reaction pathway of the ORR on Fe-$N_4$ doped graphene (black), Cu-$N_4$ doped graphene (grey), Fe-Cu diatomic sites with distance of 2.43 Å (green), and Fe-Cu diatomic sites with distance of 4.38 Å and 5.05 Å with and without phosphate.

Here, the DFT calculation evidently indicates the activity of bimetallic FeCu catalysts is closely related to the distance between atomic Fe and Cu sites, which is consistent with the experimental results of the performance of FeCu/N-CNTs with different Fe:Cu ratios. In the

FeCu system, the formation Fe-Cu dual sites with appropriate distance is important not only for the high ORR activities but also for the promotion effect of PA on ORR at the Fe sites. The high ORR performance of FeCu(4:1) in PA acid electrolyte can be contributed to the synergistic role of the close adjacent of Cu and Fe atoms with an appropriate distance, i.e., around 4~5 Å, facilitating the breakage of the O=O double bond (*OOH→*O) for ORR. This appears similar to the ORR on heme-copper oxidases (HCOs), one of the most efficient natural oxygen reduction enzyme, which contains a heme (with Fe-$N_4$ center) that functions as oxygen binding sites, and a closely associated Cu atom with a distance of 7 Å that plays the role to assist O=O double bond cleavage[63, 64]. The reduction of $O_2$ to $H_2O$ is a proton-coupled 4-electron transfer process, and the performance of electrocatalysts for ORR depends strongly on the optimized transfer of both electrons and protons[65-67]. The strongly absorbed phosphate on Cu atoms provides local protons to facilitate the ORR process. This is supported by both DFT calculation and XPS results (Figure 5E and F, Figure 6B) that phosphate ions are preferentially adsorbed on the Cu sites. The synergistic effect of the proton transfer via atomic Cu sites is consistent with the reported by Zhao et al. that the presence of phosphate ligands facilitates the formation of Cu hydrides, which is a critical initial step for attaching protons to assist the $CO_2$ reduction[68]. The phosphate promoted activity via the proton transfer of atomic Cu sites explains the high activity, lower Tafel slope and high performance and stability of FeCu(4:1) catalysts in the PA/PBI composite membrane based HT-PEMFCs. The phosphate promotion mechanism of ORR on atomically dispersed bimetallic FeCu(4:1) electrocatalysts is shown schematically in Figure 7.

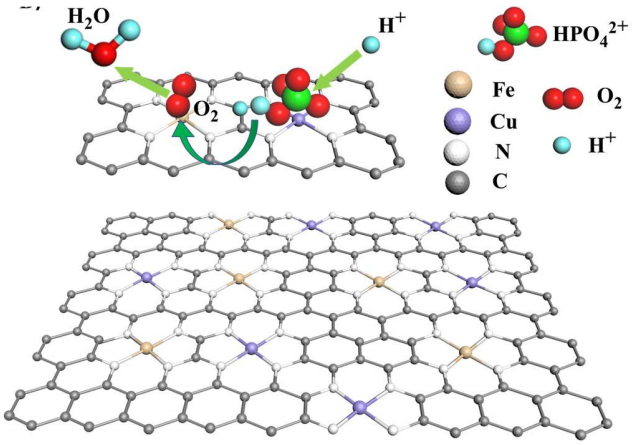


**Figure 7**. Scheme of the phosphate promoted ORR, where PA adsorbed on Cu atoms provides local protons for ORR on the adjacent Fe atoms.

## 4 Conclusion

In this work, we developed atomically dispersed bimetallic FeCu/N-CNTs catalysts with excellent activity and stability for ORR at elevated temperatures, and demonstrated for the first time that the bimetallic FeCu catalysts show surprisingly phosphate promoted ORR activity, in contrast to the PA poisoning effect of Pt/C-based electrocatalysts. On the other hand, no such phosphate promotion effect was observed on single-phased Fe SACs catalysts. The fundamental reason for the high and PA promoted activity and performance of FeCu/N-CNTs is that Cu atoms adjacent to Fe atoms with an appropriate distance (i.e., around 4-5 Å) strongly bind the phosphate, which lowers the energy barrier of Fe active sites for oxygen double bond cleavage and provides local proton to assist the proton-coupled electron transfer ORR process. The study endows that atomically dispersed FeCu bimetallic catalysts as truly Pt-free, highly active and stable cathode catalysts for PA/PBI based PEMFCs at elevated temperatures. The principles

outlined in this study open a new platform to design and develop Pt-free electrocatalysts for fuel cells in general.

**Acknowledgements**

This research was supported by the Australian Research Council under Discovery Project Funding Scheme (project number: DP180100731 and DP180100568). The authors acknowledge the facilities and the scientific and technical assistance at the Centre for Microscopy, Characterization & Analysis, the University of Western Australia, the WA X-Ray Surface Analysis Facility (project number: ARC LE120100026), and the John de Laeter Centre, Curtin University. XAS measurements were performed on the soft X-ray and XAS beamlines of the Australian Synchrotron, Victoria, Australia. The electron microscopy carried out at ORNL was supported by the U.S. Department of Energy, Office of Basic Energy Sciences and through a user proposal supported by ORNL's Center for Nanophase Materials Sciences. The DFT calculations were carried out in part at the Center for Functional Nanomaterials and the Scientific Data and Computing Center, a component of the Computational Science Initiative at Brookhaven National Laboratory, which is supported by the U.S. Department of Energy, Office of Basic Energy Sciences.

**Appendix A. Supplementary data**

Supplementary materials related to this article can be found in the online version.

**References:**

[1] S.Y. Wang, S.P. Jiang, Prospects of fuel cell technologies, National Science Review, 4 (2017) 163-166.
[2] Y. Wang, K.S. Chen, J. Mishler, S.C. Cho, X.C. Adroher, A review of polymer electrolyte membrane fuel cells: Technology, applications, and needs on fundamental research, Appl. Energy, 88 (2011) 981-1007.
[3] H.W. Zhang, P.K. Shen, Advances in the high performance polymer electrolyte membranes for fuel cells, Chem. Soc. Rev., 41 (2012) 2382-2394.

[4] J.F. Wu, X.Z. Yuan, J.J. Martin, H.J. Wang, J.J. Zhang, J. Shen, S.H. Wu, W. Merida, A review of PEM fuel cell durability: Degradation mechanisms and mitigation strategies, J. Power Sources, 184 (2008) 104-119.
[5] F. Jaouen, D. Jones, N. Coutard, V. Artero, P. Strasser, A. Kucernak, Toward Platinum Group Metal-Free Catalysts for Hydrogen/AirProton-Exchange Membrane Fuel Cells, Johnson Matthey Technology Review, 62 (2018) 231-255.
[6] J. Zhang, Y. Xiang, S. Lu, S.P. Jiang, High Temperature Polymer Electrolyte Membrane Fuel Cells for Integrated Fuel Cell – Methanol Reformer Power Systems: A Critical Review, Advanced Sustainable Systems, 2 (2018) 1700184.
[7] A. Chandan, M. Hattenberger, A. El-Kharouf, S.F. Du, A. Dhir, V. Self, B.G. Pollet, A. Ingram, W. Bujalski, High temperature (HT) polymer electrolyte membrane fuel cells (PEMFC) - A review, J. Power Sources, 231 (2013) 264-278.
[8] Q.F. Li, R.H. He, J.O. Jensen, N.J. Bjerrum, Approaches and recent development of polymer electrolyte membranes for fuel cells operating above 100 degrees C, Chem. Mat., 15 (2003) 4896-4915.
[9] J. Zhang, D. Aili, S. Lu, Q. Li, S.P. Jiang, Advancement toward Polymer Electrolyte Membrane Fuel Cells at Elevated Temperatures, Research, 2020 (2020) 15.
[10] Q. Li, J.O. Jensen, R.F. Savinell, N.J. Bjerrum, High temperature proton exchange membranes based on polybenzimidazoles for fuel cells, Progress in Polymer Science, 34 (2009) 449-477.
[11] Q. He, X. Yang, W. Chen, S. Mukerjee, B. Koel, S. Chen, Influence of phosphate anion adsorption on the kinetics of oxygen electroreduction on low index Pt(hkl) single crystals, Physical Chemistry Chemical Physics, 12 (2010) 12544-12555.
[12] Q. Li, G. Wu, D.A. Cullen, K.L. More, N.H. Mack, H.T. Chung, P. Zelenay, Phosphate-Tolerant Oxygen Reduction Catalysts, ACS Catalysis, 4 (2014) 3193-3200.
[13] Z. Liu, J.S. Wainright, M.H. Litt, R.F. Savinell, Study of the oxygen reduction reaction (ORR) at Pt interfaced with phosphoric acid doped polybenzimidazole at elevated temperature and low relative humidity, Electrochimica Acta, 51 (2006) 3914-3923.
[14] S. Kaserer, K.M. Caldwell, D.E. Ramaker, C. Roth, Analyzing the Influence of H3PO4 as Catalyst Poison in High Temperature PEM Fuel Cells Using in-operando X-ray Absorption Spectroscopy, The Journal of Physical Chemistry C, 117 (2013) 6210-6217.
[15] S. Ye, H. Kita, A. Aramata, Hydrogen and anion adsorption at platinum single crystal electrodes in phosphate solutions over a wide range of pH, Journal of Electroanalytical Chemistry, 333 (1992) 299-312.
[16] P. Zelenay, B.R. Scharifker, J.O.M. Bockris, D. Gervasio, A Comparison of the Properties of CF 3 SO 3 H and H 3 PO 4 in Relation to Fuel Cells, Journal of The Electrochemical Society, 133 (1986) 2262-2267.
[17] Y. Li, L. Jiang, S. Wang, G. Sun, Influence of phosphoric anions on oxygen reduction reaction activity of platinum, and strategies to inhibit phosphoric anion adsorption, Chinese Journal of Catalysis, 37 (2016) 1134-1141.
[18] J. Zhang, D. Aili, J. Bradley, H.H. Kuang, C. Pan, R. De Marco, Q.F. Li, S.P. Jiang, In Situ Formed Phosphoric Acid/Phosphosilicate Nanoclusters in the Exceptional Enhancement of Durability of Polybenzimidazole Membrane Fuel Cells at Elevated High Temperatures, J. Electrochem. Soc., 164 (2017) F1615-F1625.
[19] M. Lefèvre, E. Proietti, F. Jaouen, J.-P. Dodelet, Iron-Based Catalysts with Improved Oxygen Reduction Activity in Polymer Electrolyte Fuel Cells, Science, 324 (2009) 71-74.
[20] H.B. Yang, J. Miao, S.F. Hung, J. Chen, H.B. Tao, X. Wang, L. Zhang, R. Chen, J. Gao, H.M. Chen, L. Dai, B. Liu, Identification of catalytic sites for oxygen reduction and oxygen evolution in N-doped graphene

materials: Development of highly efficient metal-free bifunctional electrocatalyst, Science Advances, 2 (2016) e1501122.
[21] C.W.B. Bezerra, L. Zhang, K.C. Lee, H.S. Liu, A.L.B. Marques, E.P. Marques, H.J. Wang, J.J. Zhang, A review of Fe-N/C and Co-N/C catalysts for the oxygen reduction reaction, Electrochim. Acta, 53 (2008) 4937-4951.
[22] Q. Zhang, J. Guan, Single-Atom Catalysts for Electrocatalytic Applications, Advanced Functional Materials, 30 (2020) 2000768.
[23] L. Bai, Z. Duan, X. Wen, J. Guan, Bifunctional atomic iron-based catalyst for oxygen electrode reactions, Journal of Catalysis, 378 (2019) 353-362.
[24] L. Bai, C. Hou, X. Wen, J. Guan, Catalysis of Oxygen Reduction Reaction on Atomically Dispersed Copper- and Nitrogen-Codoped Graphene, ACS Applied Energy Materials, 2 (2019) 4755-4762.
[25] H.L. Tang, P.K. Shen, S.P. Jiang, W. Fang, P. Mu, A degradation study of Nation proton exchange membrane of PEM fuel cells, J. Power Sources, 170 (2007) 85-92.
[26] Y. Cheng, S. He, S.F. Lu, J.P. Veder, B. Johannessen, L. Thomsen, M. Saunders, T. Becker, R. De Marco, Q.F. Li, S.Z. Yang, S.P. Jiang, Iron Single Atoms on Graphene as Nonprecious Metal Catalysts for High-Temperature Polymer Electrolyte Membrane Fuel Cells, Advanced Science, 6 (2019) e1802066.
[27] A. Bhagi-Damodaran, M.A. Michael, Q. Zhu, J. Reed, B.A. Sandoval, E.N. Mirts, S. Chakraborty, P. Moenne-Loccoz, Y. Zhang, Y. Lu, Why copper is preferred over iron for oxygen activation and reduction in haem-copper oxidases, Nat Chem, 9 (2017) 257-263.
[28] Federica Poiana, Christoph von Ballmoos, Nathalie Gonska, Margareta R. A. Blomberg, Pia Ädelroth, P. Brzezinski, Splitting of the O–O bond at the heme-copper catalytic site of respiratory oxidases, Science Advances, 3 (2017) e1700279.
[29] X. Huang, J.T. Groves, Oxygen Activation and Radical Transformations in Heme Proteins and Metalloporphyrins, Chem Rev, 118 (2018) 2491-2553.
[30] H. Baumgartel, EXAFS, SEXAFS, XANES: X-Ray Absorption - Principles, Applications, Techniques of EXAFS, SEXAFS and XANES. Von D. Koningsberger und R. Prins. John Wiley & Sons Ltd., Chichester 1988. 673 S., Abb., Tab., Formeln. ISBN 0-471-87547-3, Nachrichten aus Chemie, Technik und Laboratorium, 36 (1988) 650-650.
[31] B. Ravel, M. Newville, ATHENA, ARTEMIS, HEPHAESTUS: data analysis for X-ray absorption spectroscopy using IFEFFIT, Journal of Synchrotron Radiation, 12 (2005) 537-541.
[32] B.C.C. Cowie, A. Tadich, L. Thomsen, The Current Performance of the Wide Range (90–2500 eV) Soft X‐ray Beamline at the Australian Synchrotron, AIP Conference Proceedings, 1234 (2010) 307-310.
[33] E. Gann, C.R. McNeill, A. Tadich, B.C.C. Cowie, L. Thomsen, Quick AS NEXAFS Tool (QANT): a program for NEXAFS loading and analysis developed at the Australian Synchrotron, Journal of Synchrotron Radiation, 23 (2016) 374-380.
[34] Y. Cheng, S. He, J.-P. Veder, R. De Marco, S.-z. Yang, S. Ping Jiang, Atomically Dispersed Bimetallic FeNi Catalysts as Highly Efficient Bifunctional Catalysts for Reversible Oxygen Evolution and Oxygen Reduction Reactions, ChemElectroChem, 6 (2019) 3478-3487.
[35] Y. Cheng, J. Zhang, S.F. Lu, H.H. Kuang, J. Bradley, R. De Marco, D. Aili, Q.F. Li, C.Q. Cui, S.P. Jiang, High CO tolerance of new SiO2 doped phosphoric acid/polybenzimidazole polymer electrolyte membrane fuel cells at high temperatures of 200-250 degrees C, Int. J. Hydrog. Energy, 43 (2018) 22487-22499.
[36] G. Kresse, J. Furthmüller, Efficient iterative schemes for ab initio total-energy calculations using a plane-wave basis set, Physical Review B, 54 (1996) 11169.
[37] G. Kresse, J. Furthmüller, Efficiency of ab-initio total energy calculations for metals and semiconductors using a plane-wave basis set, Computational Materials Science, 6 (1996) 15-50.

[38] J.P. Perdew, K. Burke, M.J.P.r.l. Ernzerhof, Generalized gradient approximation made simple, 77 (1996) 3865.
[39] I.C. Man, H.Y. Su, F. Calle‐Vallejo, H.A. Hansen, J.I. Martínez, N.G. Inoglu, J. Kitchin, T.F. Jaramillo, J.K. Nørskov, J.J.C. Rossmeisl, Universality in oxygen evolution electrocatalysis on oxide surfaces, 3 (2011) 1159-1165.
[40] Z. Zhang, J. Sun, F. Wang, L. Dai, Efficient Oxygen Reduction Reaction (ORR) Catalysts Based on Single Iron Atoms Dispersed on a Hierarchically Structured Porous Carbon Framework, Angewandte Chemie International Edition, 57 (2018) 9038-9043.
[41] Z. Miao, X. Wang, M.-C. Tsai, Q. Jin, J. Liang, F. Ma, T. Wang, S. Zheng, B.-J. Hwang, Y. Huang, S. Guo, Q. Li, Atomically Dispersed Fe-Nx/C Electrocatalyst Boosts Oxygen Catalysis via a New Metal-Organic Polymer Supramolecule Strategy, Advanced Energy Materials, 8 (2018) 1801226.
[42] L. Yang, D. Cheng, H. Xu, X. Zeng, X. Wan, J. Shui, Z. Xiang, D. Cao, Unveiling the high-activity origin of single-atom iron catalysts for oxygen reduction reaction, Proceedings of the National Academy of Sciences, 115 (2018) 6626-6631.
[43] J.-D. Yi, R. Xu, Q. Wu, T. Zhang, K.-T. Zang, J. Luo, Y.-L. Liang, Y.-B. Huang, R. Cao, Atomically Dispersed Iron–Nitrogen Active Sites within Porphyrinic Triazine-Based Frameworks for Oxygen Reduction Reaction in Both Alkaline and Acidic Media, ACS Energy Letters, 3 (2018) 883-889.
[44] Y. Li, Y. Zhou, C. Zhu, Y.H. Hu, S. Gao, Q. Liu, X. Cheng, L. Zhang, J. Yang, Y. Lin, Porous graphene doped with Fe/N/S and incorporating Fe3O4 nanoparticles for efficient oxygen reduction, Catalysis Science & Technology, 8 (2018) 5325-5333.
[45] J. Zhou, P.N. Duchesne, Y. Hu, J. Wang, P. Zhang, Y. Li, T. Regier, H. Dai, Fe-N bonding in a carbon nanotube-graphene complex for oxygen reduction: an XAS study, Phys Chem Chem Phys, 16 (2014) 15787-15791.
[46] Q. Li, W. Chen, H. Xiao, Y. Gong, Z. Li, L. Zheng, X. Zheng, W. Yan, W.-C. Cheong, R. Shen, N. Fu, L. Gu, Z. Zhuang, C. Chen, D. Wang, Q. Peng, J. Li, Y. Li, Fe Isolated Single Atoms on S, N Codoped Carbon by Copolymer Pyrolysis Strategy for Highly Efficient Oxygen Reduction Reaction, Advanced Materials, 30 (2018) 1800588.
[47] J. Long, W. Gang, Z. Rui, Z. Hua, Y. Shu-Hong, J. Hai-Long, From Metal–Organic Frameworks to Single-Atom Fe Implanted N-doped Porous Carbons: Efficient Oxygen Reduction in Both Alkaline and Acidic Media, Angewandte Chemie International Edition, 57 (2018) 8525-8529.
[48] C. Du, Y. Gao, H. Chen, P. Li, S. Zhu, J. Wang, Q. He, W. Chen, A Cu and Fe dual-atom nanozyme mimicking cytochrome c oxidase to boost the oxygen reduction reaction, Journal of Materials Chemistry A, 8 (2020) 16994-17001.
[49] M. Nasir, N. Patra, M.A. Ahmed, D.K. Shukla, S. Kumar, D. Bhattacharya, C.L. Prajapat, D.M. Phase, S.N. Jha, S. Biring, S. Sen, Role of compensating Li/Fe incorporation in Cu0.945Fe0.055−xLixO: structural, vibrational and magnetic properties, RSC Advances, 7 (2017) 31970-31979.
[50] G. Nam, J. Park, M. Choi, P. Oh, S. Park, M.G. Kim, N. Park, J. Cho, J.-S. Lee, Carbon-Coated Core–Shell Fe–Cu Nanoparticles as Highly Active and Durable Electrocatalysts for a Zn–Air Battery, ACS Nano, 9 (2015) 6493-6501.
[51] M. Nasir, N. Patra, D.K. Shukla, D. Bhattacharya, S. Kumar, D.M. Phase, S.N. Jha, S. Biring, P.M. Shirage, S. Sen, X-ray structural studies on solubility of Fe substituted CuO, RSC Advances, 6 (2016) 103571-103578.
[52] Z. Zheng, D. Yang, T. Li, X. Yin, S. Wang, X. Wu, X. An, X. Xie, A novel BEA-type zeolite core–shell multiple catalyst for hydrogen-rich gas production from ethanol steam reforming, Catalysis Science & Technology, 6 (2016) 5427-5439.
[53] G. Rossi, Spin Polarization of the Photoelectrons and Photon Polarization of X-Ray Absorption: Spectroscopy and Magnetometry, in: S. Mobilio, F. Boscherini, C. Meneghini (Eds.) Synchrotron

Radiation: Basics, Methods and Applications, Springer Berlin Heidelberg, Berlin, Heidelberg, 2015, pp. 539-570.
[54] J. Wang, K. Wang, F.-B. Wang, X.-H. Xia, Bioinspired copper catalyst effective for both reduction and evolution of oxygen, Nature Communications, 5 (2014) 5285.
[55] Y. Hu, J.O. Jensen, C. Pan, L.N. Cleemann, I. Shypunov, Q. Li, Immunity of the Fe-N-C catalysts to electrolyte adsorption: Phosphate but not perchloric anions, Applied Catalysis B: Environmental, 234 (2018) 357-364.
[56] H. Zhou, M. Cui, Y. Zhao, C. Wang, Q. Song, Preparation of Nitrogen and FeP Doped Carbon Nanotubes for Selective and Simultaneous Electrochemical Detection of Dihydroxybenzoic Acid Isomers, Electrochimica Acta, 242 (2017) 107-116.
[57] S.H. Noh, M.H. Seo, X. Ye, Y. Makinose, T. Okajima, N. Matsushita, B. Han, T. Ohsaka, Design of an active and durable catalyst for oxygen reduction reactions using encapsulated Cu with N-doped carbon shells (Cu@N-C) activated by CO2 treatment, Journal of Materials Chemistry A, 3 (2015) 22031-22034.
[58] M.-Y. Lee, S.-J. Ding, C.-C. Wu, J. Peng, C.-T. Jiang, C.-C. Chou, Fabrication of nanostructured copper phosphate electrodes for the detection of α-amino acids, Sensors and Actuators B: Chemical, 206 (2015) 584-591.
[59] M.K. Coggins, M.-T. Zhang, Z. Chen, N. Song, T.J. Meyer, Single-Site Copper(II) Water Oxidation Electrocatalysis: Rate Enhancements with HPO42− as a Proton Acceptor at pH 8, Angewandte Chemie International Edition, 53 (2014) 12226-12230.
[60] S. Cobo, J. Heidkamp, P.-A. Jacques, J. Fize, V. Fourmond, L. Guetaz, B. Jousselme, V. Ivanova, H. Dau, S. Palacin, M. Fontecave, V. Artero, A Janus cobalt-based catalytic material for electro-splitting of water, Nature Materials, 11 (2012) 802.
[61] J. Sun, Y.-H. Fang, Z.-P.J.P.C.C.P. Liu, Electrocatalytic oxygen reduction kinetics on Fe-center of nitrogen-doped graphene, 16 (2014) 13733-13740.
[62] F. Calle-Vallejo, J.I. Martinez, J. Rossmeisl, Density functional studies of functionalized graphitic materials with late transition metals for oxygen reduction reactions, Phys. Chem. Chem. Phys., 13 (2011) 15639-15643.
[63] S. Yoshikawa, A. Shimada, Reaction Mechanism of Cytochrome c Oxidase, Chemical Reviews, 115 (2015) 1936-1989.
[64] M. Wikström, Protonic sidedness of the binuclear iron-copper centre in cytochrome oxidase, FEBS Letters, 231 (1988) 247-252.
[65] J. Rosenthal, D.G. Nocera, Role of Proton-Coupled Electron Transfer in O–O Bond Activation, Accounts of Chemical Research, 40 (2007) 543-553.
[66] R.P. Gautam, Y.T. Lee, G.L. Herman, C.M. Moreno, E.C.M. Tse, C.J. Barile, Controlling Proton and Electron Transfer Rates to Enhance the Activity of an Oxygen Reduction Electrocatalyst, Angewandte Chemie International Edition, 57 (2018) 13480-13483.
[67] E.C.M. Tse, C.J. Barile, N.A. Kirchschlager, Y. Li, J.P. Gewargis, S.C. Zimmerman, A. Hosseini, A.A. Gewirth, Proton transfer dynamics control the mechanism of O2 reduction by a non-precious metal electrocatalyst, Nature Materials, 15 (2016) 754.
[68] J. Zhao, L. Sun, S. Canepa, H. Sun, M.N. Yesibolati, M. Sherburne, R. Xu, T. Sritharan, J.S.C. Loo, J.W. Ager Iii, J. Barber, K. Mølhave, Z.J. Xu, Phosphate tuned copper electrodeposition and promoted formic acid selectivity for carbon dioxide reduction, Journal of Materials Chemistry A, 5 (2017) 11905-11916.

**Table 1**. Summary of activation energy for each steps of ORR on Fe-$N_4$, FeCu/N-CNTs with different $d_{Fe\text{-}Cu}$ and Cu-$N_4$.

| Species | Step 1 ($^*O_2 \rightarrow {}^*OOH$)/eV | Step 2 ($^*OOH \rightarrow {}^*O$) /eV | Step 3 ($^*O \rightarrow {}^*OH$) /eV | Step 2 ($^*OH \rightarrow {}^*H_2O$) /eV |
|---|---|---|---|---|
| Fe-$N_4$ | 1.63 | 1.94 | 1.03 | 0.32 |
| $d_{FeCu}$ = 2.43 | 1.76 | 2.35 | 0.97 | -0.16 |
| $d_{FeCu}$= 4.38 | 1.64 | 1.98 | 0.99 | 0.31 |
| $d_{FeCu}$= 4.38 P | 1.81 | 1.59 | 1.19 | 0.33 |
| $d_{FeCu}$= 5.05 | 1.74 | 1.89 | 1.06 | 0.23 |
| $d_{FeCu}$= 5.05 P | 1.60 | 1.80 | 1.17 | 0.35 |
| Cu-$N_4$ | 0.22 | 0.43 | 2.58 | 1.69 |

**Graphite abstract**